Silicide characterization at alumina–niobium interfaces

J. T. McKeown · V. R. Radmilovic ·
R. Gronsky · A. M. Glaeser

Abstract Alumina–niobium interfaces formed by liquid-film-assisted joining with copper/niobium/copper interlayers exhibited microstructures that depend on the nature of the alumina components. Characterization of these interfaces in the transmission electron microscope provided insight on the relationship between interfacial microstructure and fracture performance. Interfaces between sapphire and niobium and those between high-purity (99.9%) polycrystalline alumina and niobium were free of secondary phases. However, niobium silicides were found at interfaces between lower-purity (99.5%) alumina and niobium, identified by electron diffraction analysis as the body-centered tetragonal α-Nb$_5$Si$_3$ phase. Spatially resolved compositional analysis was conducted on silicide particles at and away from the interface.
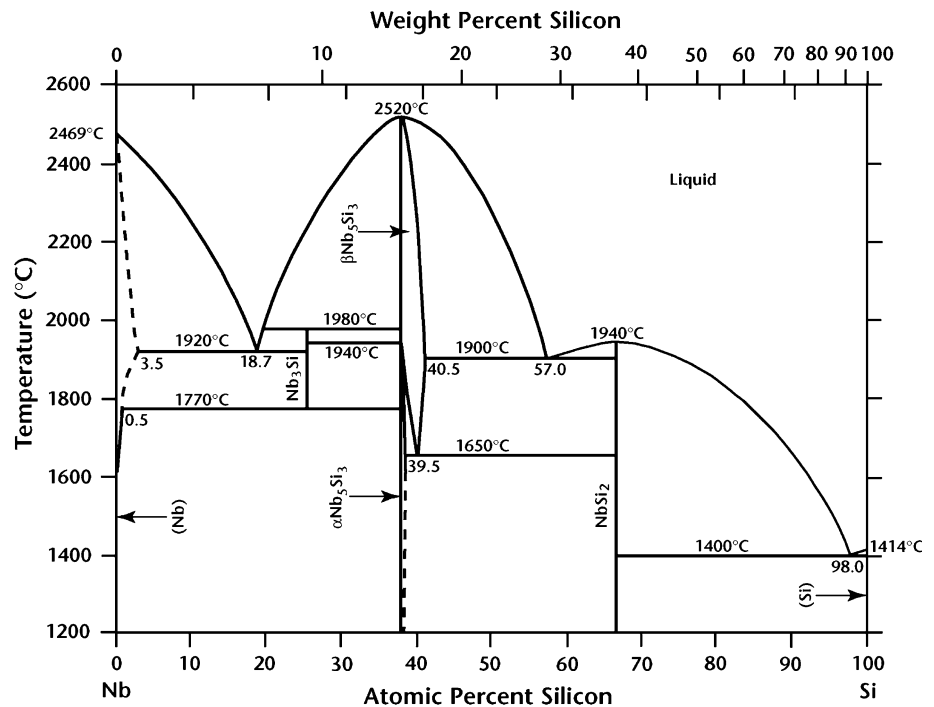
J. T. McKeown (✉)
Condensed Matter and Materials Division, Lawrence Livermore
National Laboratory, Livermore, CA 94550, USA
e-mail: mckeown3@llnl.gov

V. R. Radmilovic
National Center for Electron Microscopy, Lawrence Berkeley
National Laboratory, Berkeley, CA 94720, USA

J. T. McKeown · R. Gronsky · A. M. Glaeser
Department of Materials Science & Engineering, University of
California, Berkeley, CA 94720, USA

V. R. Radmilovic
Nanotechnology and Functional Materials Center, Faculty of
Technology and Metallurgy, University of Belgrade, Belgrade,
Serbia

Introduction

The formation of secondary phases plays an important role in both the processing and properties of fabricated ceramic–metal interfaces. Alumina (Al$_2$O$_3$)–niobium (Nb) interfaces represent a model ceramic–metal system, where the effects of interface chemistry have been studied [1–7] and interfacial Nb silicides have been previously observed [1, 6, 7]. The combination of polycrystalline Al$_2$O$_3$ and polycrystalline Nb, and their contact along an interface, results in a wide range of potential nucleation sites for silicide formation. These include Nb–Nb, Al$_2$O$_3$–Al$_2$O$_3$, and Al$_2$O$_3$–Nb grain boundaries, triple junctions involving either two Al$_2$O$_3$ or two Nb grains, and four-grain corners involving Al$_2$O$_3$ triple lines or Nb triple lines. Each type of site has a distinct spatial density and a distinct nucleation barrier that will combine to define a spectrum of nucleation frequencies. The site providing the optimum combination of energetics and spatial density will have the highest overall nucleation rate [8]. Growth rates will be influenced by the site-specific diffusion paths and Si availability, and in conjunction with nucleation rates, will determine the nature of the site or sites that dominates the overall distribution of reaction products. The properties and microstructure of such reaction products, Nb silicides in the case of interest here, can, in turn, influence the fracture path and fracture energy.

Silicide formation

Studies of Nb silicide nucleation generally involve planar "bulk" reaction couples or planar "thin-film" couples produced by depositing thin Nb films onto single-crystal Si substrates, which are subsequently annealed at various temperatures. Theoretical consideration [9–11] based on

Fig. 1 Nb–Si equilibrium binary phase diagram. Reproduced after Ref. [12]

the equilibrium phase diagram and the interfacial energies that appear in the nucleation barrier to silicide formation predict that the first crystalline silicide phase to form in the Nb–Si binary system will be $NbSi_2$ (Fig. 1 gives the Nb–Si binary equilibrium phase diagram [12]). An effective heat of formation concept [13–16] making direct use of thermodynamic data has been successful in predicting silicide phase-formation sequences in multiple metal–Si systems, as well as explaining how the presence of impurities can alter this sequence. Experimentally, the nature of the phase(s) formed depends upon the nature of the experiment performed, e.g., a thin-film versus bulk reaction couple, the specific anneal time and temperature. In thin-film studies [17–21], various stable and metastable silicide phases and phase-formation sequences have been found, depending on deposition conditions and subsequent annealing conditions. The silicides found include $NbSi_2$ [17, 18], Nb_5Si_3 [17–19], Nb_3Si [17–20], amorphous Nb silicides of varying composition [17, 18], and a body-centered orthorhombic $Nb_{11}Si_4$ phase [21]. In thin-film (and other periodic) systems, interpretation can be difficult due to limited amounts of one or more components, phases forming sequentially rather than simultaneously, and the effects of interfaces on growth and diffusion [22]. To avoid these complications, *bulk* diffusion couples of Nb–Si and Nb–$NbSi_2$ were used to study diffusion-controlled reactive growth of $NbSi_2$ and Nb_5Si_3 [22]. In Nb–Si couples, $NbSi_2$ nucleated first and grew much faster than the Nb_5Si_3 layer that developed (the $NbSi_2$ layer was ≈ 1 order of magnitude thicker than the Nb_5Si_3 layer). In both diffusion couples, an Nb_5Si_3 layer developed between the Nb and $NbSi_2$. Preliminary

experiments showed that the growth rate of Nb_5Si_3 was very low at temperatures below 1200 °C and obtaining a layer a few microns in thickness required very long anneal times.

It is to be expected that as systems under consideration become more chemically complex, further complexities can arise in the phase-formation preferences and sequences. In the interlayer used for joining, Cu is a minor constituent concentrated near the interface between the Nb-rich interlayer and a potentially silicate-containing Al_2O_3. This renders the Nb–Si–Cu system of interest. The ternary Nb–Si–Cu system has been investigated in both thin-film reaction couples [23] and "bulk" phase-equilibria studies [24, 25]. In the thin-film study, the phases formed and their formation sequence again depended on the experimental conditions. The observed phases were processing-dependent subsets of ternary $Nb_5Cu_4Si_4$ and binary Cu_3Si, $NbSi_2$, Nb_5Si_3, and Nb_3Si phases. The presence of Cu at the Nb–Si interface was found to affect the onset temperature for $NbSi_2$ and Nb_5Si_3 formation.

Isothermal sections of the ternary Nb–Si–Cu phase diagram are available at 1500, 875, and 800 °C. Figure 2 shows the 1500 °C isothermal section. It should be noted that, according to the Nb–Cu binary phase diagram [12], there is very low solubility of Cu in Nb and Nb in Cu. The Nb_5Si_3 and $NbSi_2$ phases dissolve ≈ 4 at.% Cu in the temperature range 800–875 °C. The ternary tetragonal $Nb_5Cu_4Si_4$ phase was found to form only upon rapid cooling from the melt or by solid-state diffusion (as occurred in the thin-film diffusion couples) [24]. This phase had previously been observed at 800 °C [26] and
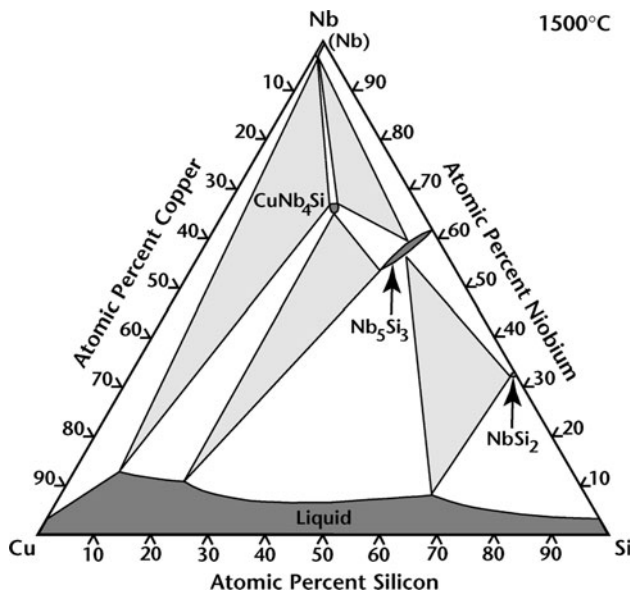
Fig. 2 Ternary Nb–Si–Cu equilibrium phase diagram at 1500 °C. Single-phase regions are shaded *dark gray* and labeled, two-phase regions are *white*, and three-phase regions are shaded *light gray*. Reproduced after Refs. [25, 71]

this observation was confirmed in a later study [25]. A tetragonal Nb_4CuSi phase has been observed at 1500 °C, in equilibrium with pure Nb and Nb_5Si_3 [25].

Intergranular glassy phase in alumina

The presence of a Si-containing intergranular glassy phase in Al_2O_3 has been shown to cause the formation of Nb silicide at Nb–Al_2O_3 interfaces [1, 6, 7]. Intergranular phases and films have been the subject of numerous investigations (as reviewed in Ref. [27]). Many have focused on Al_2O_3-based materials (e.g., [28–34]). Efforts have been made by Dillon et al. [32–34] to relate and categorize the effects of grain boundary "phases" on grain growth and transport kinetics along grain boundaries. In Al_2O_3 six distinct types of kinetic behavior were identified, each associated with a particular grain boundary "phase" that produced a characteristic grain boundary transport rate. These characteristic rates would, in turn, be expected to affect the mobility of impurities such as Nb along grain boundaries.

The wetting behavior, structure, and composition of a grain boundary in a system containing a glassy phase are generally determined by the boundary misorientation of adjacent grains [29, 30]. The majority of grain boundaries are wetted by a silicate glass phase, while low-angle and special (twin-related) boundaries are not wet. A continuous intergranular glass phase is present at higher-energy boundaries. Isolated pockets of glassy phase and continuous films containing pockets at growth ledge steps and faceted grain boundaries have been observed [30, 31]. These could potentially serve as preferred nucleation sites for secondary phases.

It was proposed [35] that migration of an intergranular glass phase to a free surface (or interface) is driven by differences in wetting behavior of the surface (or interface) and the boundary, and this was observed for specific misorientations of sapphire bicrystals [29]. Intergranular films at metal–ceramic interfaces [31] that form as a result of an intergranular glass phase in alumina were found to have the same characteristic features as intergranular films at ceramic grain boundaries. The metal played an important role in determining the film chemistry and thickness, as well as the composition of glass pockets at triple junctions. Intergranular phases may affect the preferred nucleation sites for second phases and their growth kinetics.

Mechanical properties

In idealized systems in which two phases are in contact and form bimaterial interfaces, thermal-expansion mismatches can establish residual stresses that alone or in combination with applied stresses cause failure at or near the interface (see, e.g., [36]). Even when the coefficients of thermal expansion (CTEs) are closely matched, as is the case for Al_2O_3 and Nb, differences in other physical properties will affect the fracture path and resulting fracture energy.

Fracture at a bimaterial interface is generally described by the complex stress-intensity factor [37–39], K, in which the elastic mismatch across the interface is expressed using the nondimensional Dundurs parameters [40], α and β. It was noted by Kruzic et al. [6] that in sandwich-type specimens, for which complex stress-intensity solutions exist [41], analysis is complicated by deviations of cracks from the interface [42] and the validity of these solutions breaks down at distances ahead of the crack tip [43]. Using the strain energy release rate, G, in mode I loading to evaluate crack driving forces [6] avoids these complications. In addition, G is easy to compute, invariant with respect to crack position, and unaffected by the presence of the interlayer in sandwich specimens when the interlayer thickness is small compared with other relevant specimen dimensions [41].

Cannon et al. [44, 45] determined that while linear-elastic calculations predict crack propagation along a path with maximum G and to be dependent on the Dundurs parameters (modulus mismatch), this analysis has limitations when applied to bimaterial systems and microstructural effects are important. Engineering interfaces with enhanced toughness involves generating plasticity in the metal interlayer, the competition between microstructurally weak crack paths and paths of maximum driving force, and encouraging crack jumping across the metal interlayer and

crack meandering. At Al_2O_3–Nb interfaces, it is expected that cracks that initiate close to the interface will be drawn to the Nb interlayer. The detailed crack path and fracture energy will depend on interlayer thickness and yield strength, as well as microstructural and chemical characteristics of the interface.

In the samples employed in the current study, Nb silicides along the ceramic-interlayer interface have the potential to provide microstructural weak links and can generate localized residual stresses that interact with an advancing crack. Nb silicides are brittle at room temperature. Vickers hardness values of 5.6–9.5 GPa [46] and K_{IC} values of 2.3–5.5 $MPa\sqrt{m}$ [46, 47] were measured for pure Nb_5Si_3 samples. If one assumes an elastic modulus of 188 GPa for Nb_5Si_3 [48], the K_{IC} values would imply mode I fracture energies, G_{IC}, of 28–161 J/m^2. Investigations of the fracture energy of heterophase interfaces involving Nb silicide [49] found the interfacial fracture energy of Al_2O_3 with Nb_5Si_3 to be ≈ 16 J/m^2, while the interfacial fracture energy between Nb and Nb_5Si_3 was found to exceed 34 J/m^2.

Effects of silicides at processed interfaces

Even in a "simple" system such as Nb–Si, a range of phases and phase distributions develop in multilayer systems. The associated microstructural differences have the potential to induce differences in the response to loading, specifically, the fracture path and fracture energy.

In the Al_2O_3–Nb system, the potential Si source is an intergranular glassy phase in the Al_2O_3. In fracture studies of Al_2O_3–Nb interfaces in which the Al_2O_3 was heavily contaminated with silicate (97% pure Al_2O_3) [1], Nb embrittlement due to oxygen uptake was augmented relative to assemblies using higher-purity Al_2O_3 by flow of Si/silicate to the Al_2O_3–Nb interface. Patches of Nb silicide (Nb_4Si) were identified on fracture surfaces of specimens that failed within the Nb. These patches extended into the Nb in the vicinity of the Al_2O_3–Nb interface.

Collective observations from studies of Al_2O_3–Nb interfaces fabricated with Cu/Nb/Cu interlayers [6, 50–53] indicate a substantial sensitivity of the fracture behavior to the processing temperature, bonding atmosphere, interlayer design, post-bonding heat treatments, and testing method, even in situations where, from a macroscopic perspective, the system is approximated as an Al_2O_3–Nb bond (a bimaterial interface) and the *same* Al_2O_3 is used throughout. This suggests that the interfacial microstructure is sensitive to the details of the processing, and that changes in the processing parameters, broadly defined, influence the interplay between fracture paths of maximum driving force and those of microstructural weakness. Changes in the nature of the Al_2O_3 add further complexity. This work was undertaken in part to more fully characterize the nature of the ceramic–metal interfaces generated, particularly the interface between an Al_2O_3 containing an intergranular glassy phase and a Nb-based interlayer, and relate the observed microstructures to the fracture characteristics of the interfaces.

Experimental procedures

The materials and experimental procedures used to produce samples for the characterization studies described herein are identical to those used in prior studies to produce joined samples with Cu/Nb/Cu interlayers. Three types of Al_2O_3 were used: an undoped, high-purity, single-crystal, (0001)-oriented sapphire ($\approx 99.996\%$ pure, Insaco Inc., Quakertown, PA, USA); a high-purity, high-strength, fine-grain-size polycrystalline Al_2O_3 ($\approx 99.9\%$ pure, SSA-999W, Nikkato Corp., Osaka, Japan); and a lower-purity, lower-strength, coarser-grain-size polycrystalline Al_2O_3 ($\approx 99.5\%$ pure, AD995, Coors Technical Ceramic Co., Oak Ridge, TN, USA). The 99.9% pure material had a uniform microstructure with an average (mean linear intercept) grain size of ≈ 1 μm; the 99.5% pure Al_2O_3 exhibited a bimodal grain-size distribution, with the larger grains roughly 25 μm in size and the finer-grained regions typically consisting of grains ≈ 5 μm or less in size.

The as-received sapphire was polished to an optical finish. Surface roughness measurements using contact profilometry yielded average R_a values of 0.0036, 0.0037, and 0.0108 μm for line scans of 50, 500, and 5000 μm, respectively. The bonding surfaces of polycrystalline Al_2O_3 blocks were first ground flat with a 400 grit (37 μm) diamond wheel, then polished with successively finer-grit diamond (9, 6, 3, and 1 μm) paste and finished with 0.02 μm colloidal silica suspension. For the polycrystalline samples, average R_a values for line scans of 50, 500, and 5000 μm were 0.0089, 0.0105, and 0.0784 μm, respectively. The polished surfaces of the Al_2O_3 substrates were coated with ≈ 3.0-μm-thick Cu films. The coated Al_2O_3 substrates were joined using a 125-μm-thick Nb foil ($\approx 99.99\%$ pure, Goodfellow Corp., Malvern, PA, USA) in a graphite-element hot press. A bonding pressure of ≈ 2 MPa was maintained for 6 h at 1400 °C under a vacuum of $\approx 10^{-2}$ Pa (10^{-7} atm). In-depth processing details are available in previous publications [50–55].

Cross-sectional TEM specimens of the interfaces were prepared by conventional grinding, polishing, and dimpling techniques. The thin foils were perforated using a low-energy Ar^+ ion mill. Conventional TEM (imaging and diffraction analysis) was performed on a JEOL 200CX and a JEOL 2011 operating at 200 keV. Elemental analysis using energy-dispersive spectrometry (EDS) was performed on a Philips CM200 FEG (S)TEM operating at 200 keV with a probe size of 2 nm.

Results and discussion

The solubility–diffusivity product for Cu in Nb is sufficiently low at the bonding temperature (1400 °C) that, for a bonding time of 6 h, discrete particles of residual Cu decorate the sapphire–Nb and Al_2O_3–Nb interfaces. The morphology and projected (plan view) area fraction of these ductile interfacial Cu particles influence the extent of toughening obtained through metal plasticity and particle tearing, and thereby affect the fracture strength of the joined assemblies [6, 7, 49, 52, 56]. The ultimate spatial distribution of Cu along the ceramic-interlayer interface will depend upon the bonding temperature, pressure, and time, the bonding-surface roughness, and the microstructure and chemistry of the bulk ceramic [7, 51–53, 55, 57]. Well-polished samples with R_a much less than the Cu film thickness, fabricated using the same bonding conditions, were selected to isolate the effects of Al_2O_3 microstructure and purity.

Prior work has shown that in all three types of samples, the area fraction of residual Cu particles at the ceramic-interlayer interface is typically $\leq 5\%$ for the processing conditions described. As a result, a plan view of the ceramic-interlayer interface is well suited to detecting and characterizing the Cu particle size and distribution. Comparisons of sapphire-interlayer interfaces and polycrystalline Al_2O_3-interlayer interfaces reveal that the sizes and distributions of particles are affected by the ceramic microstructures. Specifically, the average size of Cu particles, and to a lesser degree the projected area fraction, decreases with the grain size. This, coupled with observations of the fracture-surface topography, suggests that grain-boundary grooving in both the metal foil [7, 55] and on the ceramic surface plays a role in defining the average size and spacing of the Cu particles. Decreasing the average Cu particle size will in turn increase the amount of Cu-interlayer contact area per unit area of interface, which may increase the total flux of Cu into the Nb core layer and contribute to decreasing area fractions of Cu with decreasing Al_2O_3 grain size.

As a result of the low area fraction of Cu particles, assumed to be ≤ 0.05, the average nearest-neighbor particle separation distance is estimated to be of the order of ≥ 3–$5\times$ the average particle diameter (≈ 10 μm in samples using sapphire substrates to ≤ 1 μm in samples using high-purity Al_2O_3 substrates). A *random* cut perpendicular to the plane of the interface, designed to allow a cross-sectional view, will generally intersect relatively few and widely separated particles. In an SEM, it is possible to view in cross-section an interface that is multiple millimeters in length, and those segments in which particles are intersected can be examined. In the TEM work described here, a typical length of ceramic-interlayer interface is in the range
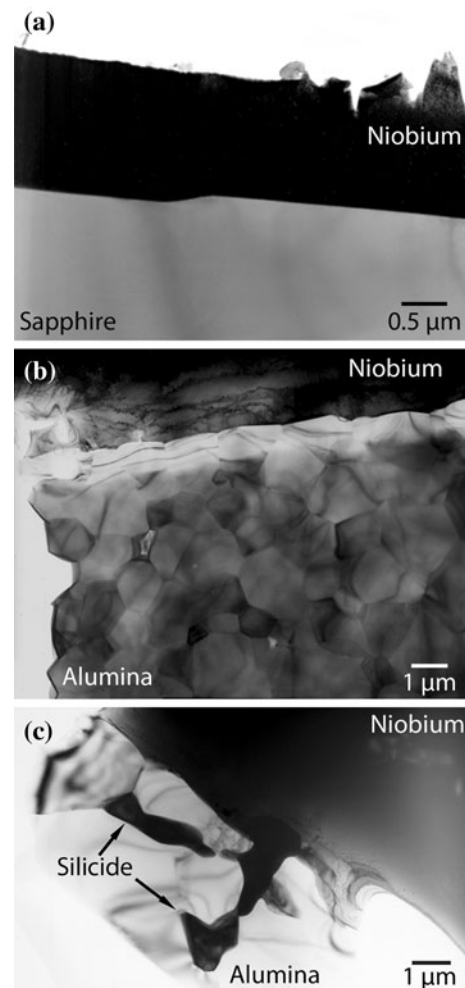
Fig. 3 Bright-field TEM images of **a** a (0001) sapphire–Nb interface, **b** a high-purity Al_2O_3–Nb interface (note the preferential thinning at the interface), and **c** a lower-purity Al_2O_3–Nb interface revealing the presence of Nb silicides

of 2–20 μm. It follows that the likelihood of a particle intersection is very low. This is consistent with our observations (or lack thereof). Moreover, due to the relatively higher milling rate of Cu, even when Cu particles are intersected, there is a high likelihood that preferential etching of a through-thickness particle will generate a particle-shaped perforation along the ceramic-interlayer interface. Isolated observations of such features have been made.

In view of the understandable absence of Cu particles, the primary differences in the interfacial microstructures and chemistries among the three types of samples fabricated reflect the effects of the Al_2O_3 microstructure on the interface "roughness" and of the Al_2O_3 chemistry on Al_2O_3-interlayer compatibility and the potential for reaction-product formation along the interface. Figure 3 presents bright-field TEM images of the three types of fabricated interfaces for comparison of the microstructures.

Figure 3a shows a (0001) sapphire–Nb interface. The interface appears distinct and smooth with no reaction phases present [3, 55, 58, 59], as sapphire eliminates the possibility of a glassy phase flowing to and filling interfacial voids [55]. EDS confirmed that silicides and other secondary phases were not present at the sapphire–Nb interface.

Figure 3b shows a bright-field TEM image of a high-purity Al_2O_3–Nb interface. Again, there was no evidence of silicide or other secondary-phase formation at the interface, as expected for a high-purity Al_2O_3. EDS confirmed this. The interface appears "rough" relative to the sapphire–Nb interface due to grooving of the fine-grained Al_2O_3 during the bonding cycle, with the Nb conforming to the Al_2O_3 grain-boundary grooves. This roughness was even more evident in fracture surfaces when joined assemblies prepared from this Al_2O_3 failed along the ceramic-interlayer interface [55]. As observed in previous studies [60–62], preferential thinning of the interface occurs during TEM specimen preparation.

Figure 3c reveals the microstructure along a lower-purity Al_2O_3–Nb interface. Again, the Nb has conformed to the Al_2O_3 grain-boundary grooves, and the interface appears "rough" relative to the single-crystal sapphire–Nb interface. Nb silicides are evident at and slightly away from the Al_2O_3–Nb interface, consistent with previous studies [6, 7] in which Nb-silicide formation was observed in small-grained regions of the Al_2O_3. This higher grain-boundary density in these regions leads to a higher flux and local concentration of Si per unit area of Al_2O_3 at the interface as the glassy silicate phase present at Al_2O_3 grain boundaries flows to the interface. Chemical analysis using EDS [6, 7] indicated a Nb:Si ratio of $\approx 4.5/3$ (≈ 1.5) and the silicide particles were determined to be the Nb_5Si_3 phase (see Fig. 1). At these interfaces, nucleation likely occurred where Nb metal was in contact with Al_2O_3 grain boundaries, and thus silicate that flowed to the interface. Formation of pockets at triple lines involving two Nb–Al_2O_3 and one Al_2O_3–Al_2O_3 grain boundary and four-grain junctions where three Al_2O_3–Al_2O_3 and one Nb–Al_2O_3 interface come together will produce larger localized reservoirs of Si (silicate). The proximity of these pockets to the Nb source suggests that nucleation should be preferred at the interface rather than at subsurface triple lines or four-grain junctions.

Silicide formation requires a sufficiently low O_2 activity; the equilibrium O_2 partial pressure to form Nb_5Si_3 from a reaction between pure SiO_2 and Nb is of the order of 10^{-14} atm (10^{-9} Pa) at 1400 °C. The O_2 partial pressure for Nb–NbO equilibrium at 1400 °C is $\approx 6 \times 10^{-18}$ atm (6×10^{-13} Pa) at 1400 °C [63]. The Nb foil is thus expected to establish a low O_2 activity along the Al_2O_3–Nb interface, which in turn promotes the reaction of an intergranular silicate with Nb to form a silicide in the near-interfacial region. Moreover, oxygen readily dissolves in and is a fast diffuser in Nb [64, 65]. The dissolution makes the reaction more favorable, and the rapid diffusion prevents a build-up of dissolved oxygen at the interface. The graphite-element environment coupled with a 10^{-7} atm (10^{-2} Pa) vacuum pressure during bonding is expected to establish a sufficiently low ambient O_2 pressure to allow oxygen removal from the foil edges. Under these conditions, the observed formation of interfacial silicides is expected.

The local microstructure seen in Fig. 3c suggests that following nucleation the particles grew into the Al_2O_3 along grain boundaries, where the Si concentration will be higher as the reaction progresses. The silicide particles also grew laterally along the Al_2O_3–Nb interface and slightly into the Nb. Lateral expansion of the silicide along the Al_2O_3–Nb interface is likely due to enhanced diffusion of Si along the Al_2O_3-silicide boundary or flanking Al_2O_3–Nb boundary, as the rate of diffusion along this boundary can be expected to be much greater than diffusion of Si through the silicide lattice. Faceting at the interface between Nb and the Nb silicide was observed (see, for example, Fig. 7a), which may limit the growth rate of the silicide into the Nb foil. Grain boundaries in the silicide particles suggest multiple nucleation sites along Al_2O_3 grain boundaries.

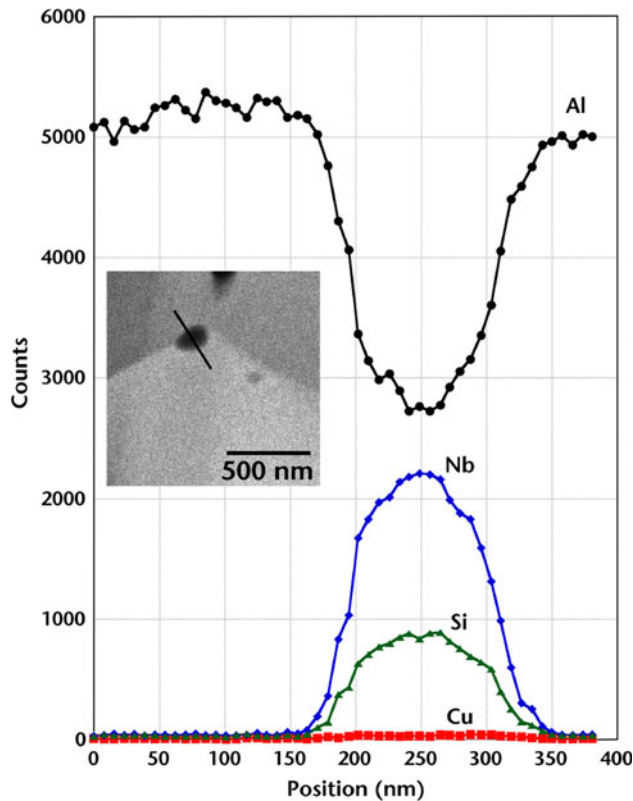Chemical analysis was performed on silicide particles at and away from the Al_2O_3–Nb interface using EDS in the TEM. Figure 4a shows EDS spectra obtained from multiple regions of a silicide particle at the interface. The spectra show the presence of Nb, Si, and Cu, and no dissolved Al in the particle. When the spectra are normalized by their maximum Nb_L counts to reduce specimen-thickness effects, the normalized spectra overlap, indicating constant Nb:Si and Nb:Cu ratios in the silicide particle. Figure 4b presents an EDS line scan across the silicide particle. The dashed line in the figure indicates the position of the interface between the Nb metal and silicide particle. The interface does not appear distinct due to the combined effects of specimen thickness and tilting of the interface (the interface is not edge-on) relative to the incident electron beam. Minimizing these thickness effects was again achieved by normalizing the Cu and Si counts by the Nb counts at each position in the scan. The Nb:Si and Nb:Cu ratios appear constant across the silicide particle. The nominal composition of this particle was 54 (± 2) at.% Nb, 40 (± 2) at.% Si, and 6 (± 5) at.% Cu, with a Nb:Si ratio of 1.35. The presence of dissolved Cu is a result of the cladding layers of the interlayer used to join the Al_2O_3.

Small, isolated particles on Al_2O_3 grain boundaries away from the Al_2O_3–Nb interface, believed to have formed during cooling from the processing temperature [7],
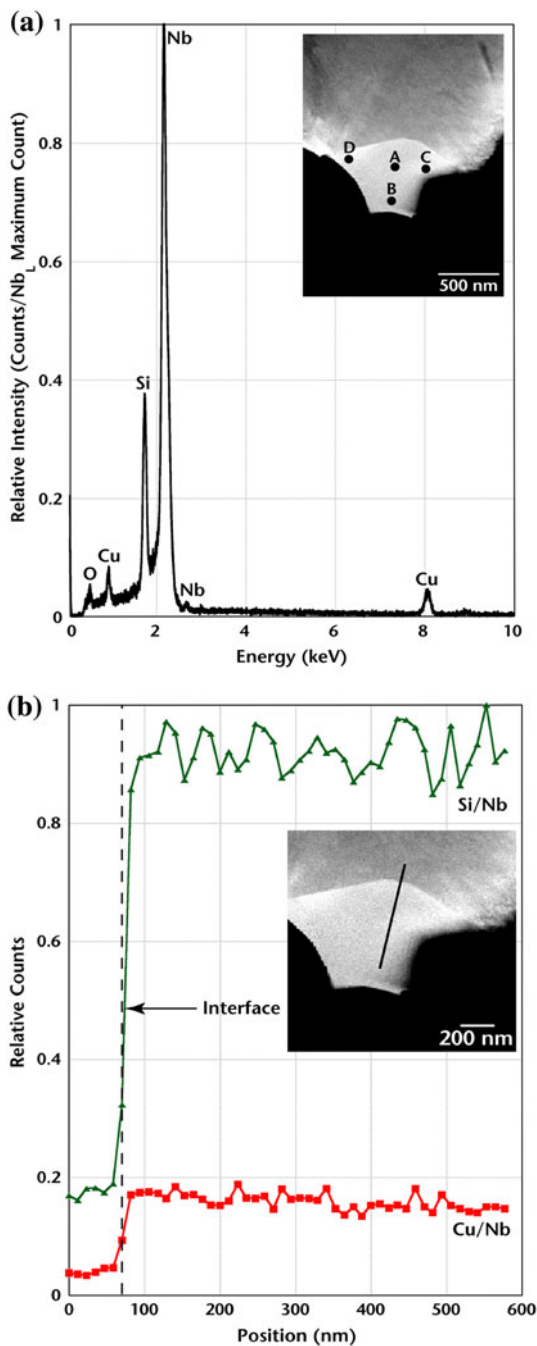
Fig. 4 **a** EDS spectra from four different regions of a silicide particle at the Al$_2$O$_3$–Nb interface, and **b** line scan across the particle. When normalized by the Nb counts to minimize thickness effects, **a** the four spectra overlap and **b** the Cu and Si concentrations are constant across the scanned region of the particle. The *dashed line* in **b** indicates the interface between the Nb and the silicide particle


Fig. 5 EDS line scan across a small silicide particle on an Al$_2$O$_3$ grain boundary, showing the presence of Nb, Si, and Cu

were also analyzed. Figure 5 shows an EDS line scan across a particle that lies ≈1 μm from the Al$_2$O$_3$–Nb interface, with the associated HAADF image. The EDS scan again reveals the presence of Nb, Si, and trace amounts of Cu. Figure 6 shows an EDS spectrum obtained from a particle ≈500 nm from the Al$_2$O$_3$-interlayer interface. The nominal composition of the particle was 52 (±4) at.% Nb, 43 (±4) at.% Si, and 5 (±10) at.% Cu, giving a Nb:Si ratio of 1.21. The accuracy of compositions obtained from particles along Al$_2$O$_3$ grain boundaries are likely skewed by the Al$_2$O$_3$ that partially envelops the silicide particle, which produced Al and O signals, as seen in Fig. 6, along with Nb, Si, and Cu. The uncertainty in the estimated Cu level is perhaps symptomatic of the difficulties. In view of this, the shift in the Nb:Si ratio to 1.21 relative to that of the silicides closer to the Al$_2$O$_3$-interlayer interface (Nb:Si of 1.35) must be viewed with caution.

In order to accurately determine the specific Nb-silicide phase, crystallographic analysis was conducted using electron diffraction. Based on the Nb:Si ratios, which will be further discussed subsequently, attention turned to the Nb$_5$Si$_3$ phase. There are two stable allotropes of Nb$_5$Si$_3$, both with a body-centered tetragonal crystal structure (space group I4/mcm): α-Nb$_5$Si$_3$ is stable below 1940 °C with lattice parameters a = 6.571 Å and c = 11.889 Å while β-Nb$_5$Si$_3$ is stable above 1650 °C with lattice parameters a = 10.018 Å and c = 5.072 Å [12, 66, 67]. Metastable γ-Nb$_5$Si$_3$ is hexagonal (space group P6$_3$/mcm) with lattice parameters a = 7.536 Å, c = 5.249 Å, and γ = 120° and has been found to be stabilized by interstitial impurities, particularly C [66, 67]. As a specific example of
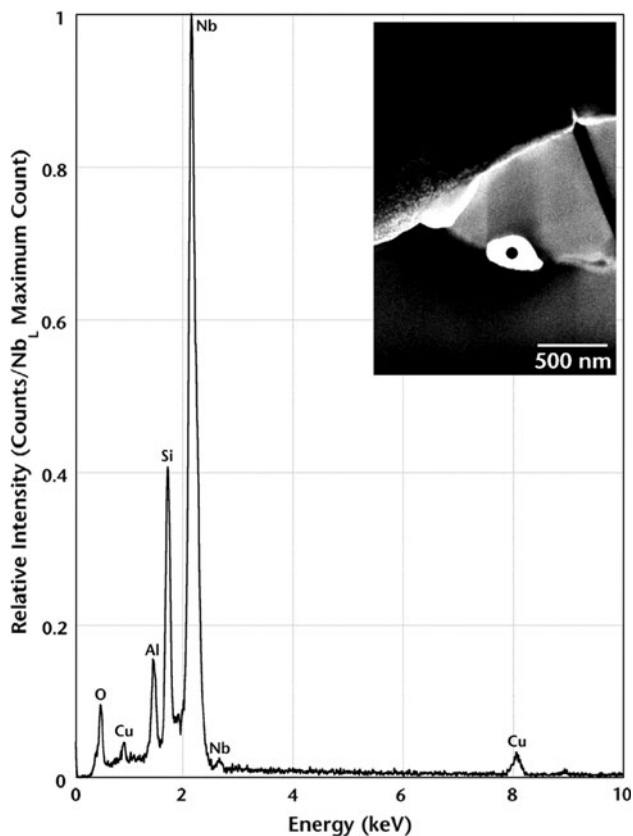
Fig. 6 EDS spectrum obtained from a silicide particle along an Al_2O_3 grain boundary away from the Al_2O_3–Nb interface

stabilization by interstitial impurities, the addition of Hf was found to stabilize γ-Nb_5Si_3 up to 1500 °C [68]. At the processing temperature employed in this study, $NbSi_2$, with a hexagonal crystal structure (space group $P6_222$) and lattice parameters $a = 4.819$ Å, $c = 6.592$ Å, and $\gamma = 120°$, is also stable [66]. In diffusion couples involving bulk Nb/Si and bulk $Nb/NbSi_2$ phases in the temperature range from 1200–1350 °C, only $NbSi_2$ and Nb_5Si_3 formed [22]. Similarly, in samples prepared by field-activated pressure-assisted combustion synthesis of elemental Nb and Si powders at 1400 °C, either Nb_5Si_3 or a combination of Nb_5Si_3 and $NbSi_2$ were formed [46]. We note that reports of multiple other phases exist in the literature, but the phases appear in samples processed either at higher or lower temperatures. Nb_3Si appears in the binary phase diagram between 1770 and 1980 °C, and both stable tetragonal primary Nb_3Si [20, 69] and finer metastable orthorhombic Nb_3Si particles [20] have been observed in solidified materials, but these materials were processed at higher temperatures than the joints produced for this study. A body-centered orthorhombic $Nb_{11}Si_4$ [21] phase has recently been reported to form as a precipitate in Nb–Si solid solutions. The tetragonal $Nb_5Cu_4Si_4$ phase has been reported in both phase-equilibria studies [25] and thin-film

reaction couples [23] processed at temperatures lower than the bonding temperature used in the present work. Additionally, tetragonal Nb_4CuSi [25] has been observed. Consequently, it was desirable to identify the crystallographic form(s) of the silicides in our material.

The silicide particle shown in Fig. 4, from which EDS data was obtained, was chosen for crystallographic analysis. The lateral expansion of the silicide particle at the interface decreases the likelihood of surrounding Al_2O_3 or Nb either above or below the silicide through the thickness of the TEM foil. The bright-field image in Fig. 7a shows the silicide particle, recorded in the [001] zone axis. There was no low-index plane-on-plane orientation relationship between this specific silicide and Nb pair, nor was any preferred orientation relationship evident for any silicide particles along the interface or alumina grain boundaries. This may have implications as to whether the silicide phase nucleated on one of the "substrate" phases (Nb or Al_2O_3) or within the glassy phase. Examinations of Nb–Al_2O_3 fracture surfaces using Auger electron spectroscopy [6] suggest that the glassy phase does not wet the Nb–Al_2O_3 interface and is largely confined to pockets. Experiments of the type performed in Refs. [29–31] may be better suited for determining whether the glassy phase wets the silicide/contacting-phase interface. If the glassy phase wets this interface, nucleation may occur within the glass pocket. If the silicide nucleated within the glassy phase, no preferred orientation relationship would be expected.

Four experimental zone-axis diffraction patterns were obtained, presented in Fig. 7b; these zone axes are, as indicated in the figure, [001], [111], [211], and [201]. The diffraction patterns are superimposed on a quadrant of the (001) stereographic projection of a tetragonal crystal, which also illustrates the relation between the four orientations. The four respective simulated zone-axis diffraction patterns for the α-Nb_5Si_3 phase are shown in Fig. 7c, and they are consistent with the experimental diffraction data. The diffraction analysis revealed the silicide particle to be the low-temperature body-centered tetragonal α-Nb_5Si_3 phase, confirming prior EDS results [6, 7] that found a Nb:Si ratio consistent with Nb_5Si_3.

Although EDS analysis indicated differing Nb:Si ratios in the silicides at and slightly away from the ceramic-interlayer interface, no difference in their crystal structures was evident. The small size of intergranular silicides, combined with the lack of a preferred orientation relationship between the silicide and either of the adjoining, misoriented Al_2O_3 grains, introduced diffraction from the surrounding Al_2O_3 matrix that complicated diffraction analysis. Figure 8 shows bright-field and dark-field images of a small silicide particle ≈ 500 nm from the Al_2O_3-interlayer interface. Diffraction patterns revealed this particle to also be the α-Nb_5Si_3 phase. The images were
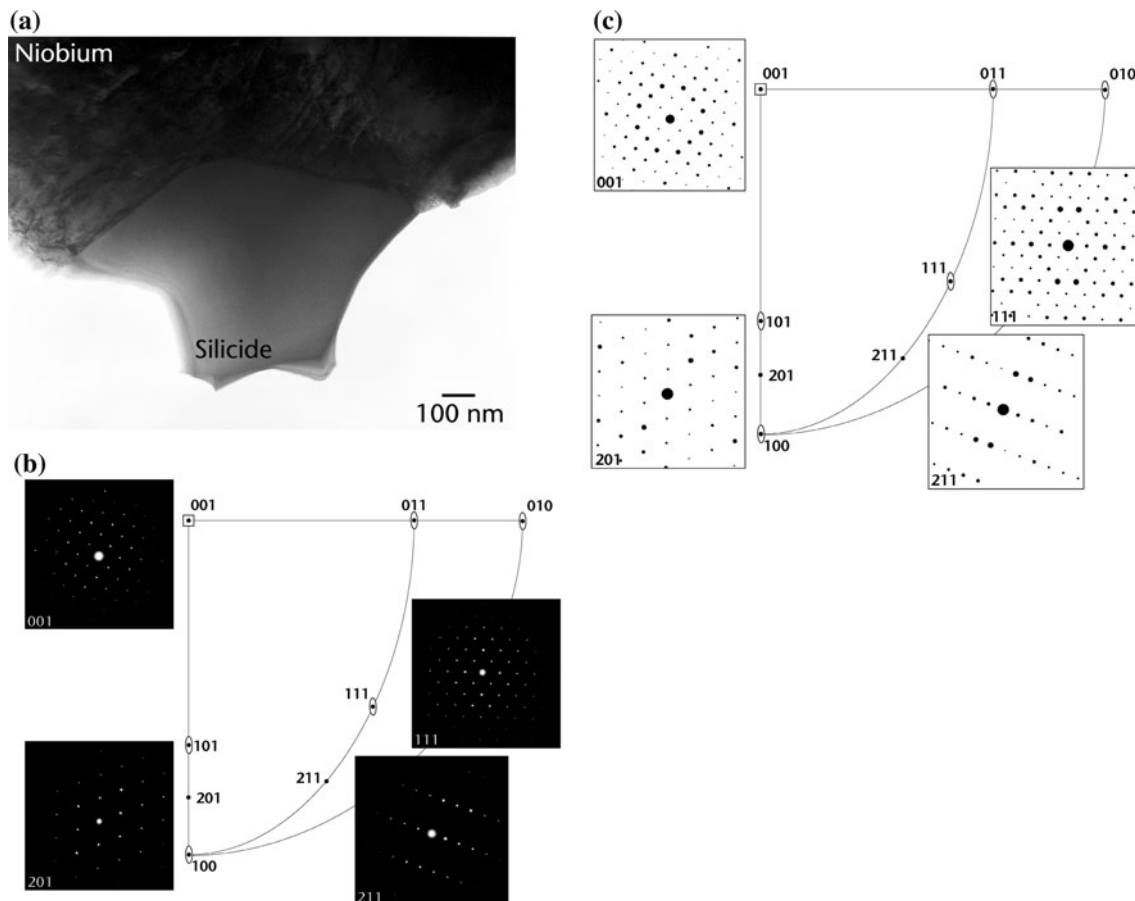
Fig. 7 a Bright-field TEM image of the silicide particle from which the diffraction patterns in **b** were obtained. The image was recorded in the [001] zone axis. **b** Experimental and **c** simulated [001], [111], [211], and [201] zone-axis diffraction patterns for the particle shown in **a**, superimposed on a quadrant of the (001) stereographic projection for a tetragonal crystal, revealing that the particle is the body-centered tetragonal Nb_5Si_3 phase

obtained by tilting into a (200) systematic row condition from the [001] zone axis, as shown in the diffraction patterns inset in the figures.

In view of the presence of Nb, Si, and, to a more limited degree, Cu in the silicide particles, the Nb:Si ratios and the overall compositions were assessed in the context of the available Nb–Si and Nb–Si–Cu phase diagrams. The measured Nb:Si ratios, 1.35 and 1.21, place the composition within the two-phase field between Nb_5Si_3 and $NbSi_2$ on the binary equilibrium phase diagram. Two experimental studies [24, 25] of phase equilibria in the Nb–Si–Cu system are available. Experimental evidence indicates that Nb_5Si_3 can incorporate up to 12 at.% Cu at 1500 °C [25]. At 1500 °C, the nominal silicide compositions lie in the two-phase field between Nb_5Si_3 and $NbSi_2$ on the ternary phase diagram (Fig. 2), close to the Nb_5Si_3 single-phase region. As the temperature is decreased, phase boundary shifts are expected. The maximum Cu solubility in the Nb_5Si_3 phase at 1100 °C was estimated as 4 at.%. The 875 and 800 °C isothermal sections suggest changes in the

nature of the phases that would coexist in a system having the nominal particle compositions, and a substantially lower solubility of Cu in Nb_5Si_3 than at 1500 °C. At 875 °C, the compositions would lie in a three-phase stability field of Nb_5Si_3, $NbSi_2$, and a ternary liquid; the phase diagram suggests a solubility limit of Cu in Nb_5Si_3 of ≈ 2 at.% [24]. At 800 °C, the nominal compositions would lie in a three-phase stability field of Nb_5Si_3, $NbSi_2$, and Cu_3Si, with the Nb_5Si_3 phase incorporating up to ≈ 2–3 at.% Cu [24].

The EDS results, when assessed in the context of available phase diagrams, predict a multiphase equilibrium microstructure. However, evidence of silicide phases other than the Nb_5Si_3 phase was not found using electron diffraction. Contrast in bright-field images also did not reveal a second silicide phase, either within the Nb_5Si_3 particles or at the interfaces between Nb_5Si_3 particles with the Al_2O_3 and Nb. While it is possible that a much more extensive examination of silicide particles (a dozen were examined using electron diffraction) may reveal other phases, a key
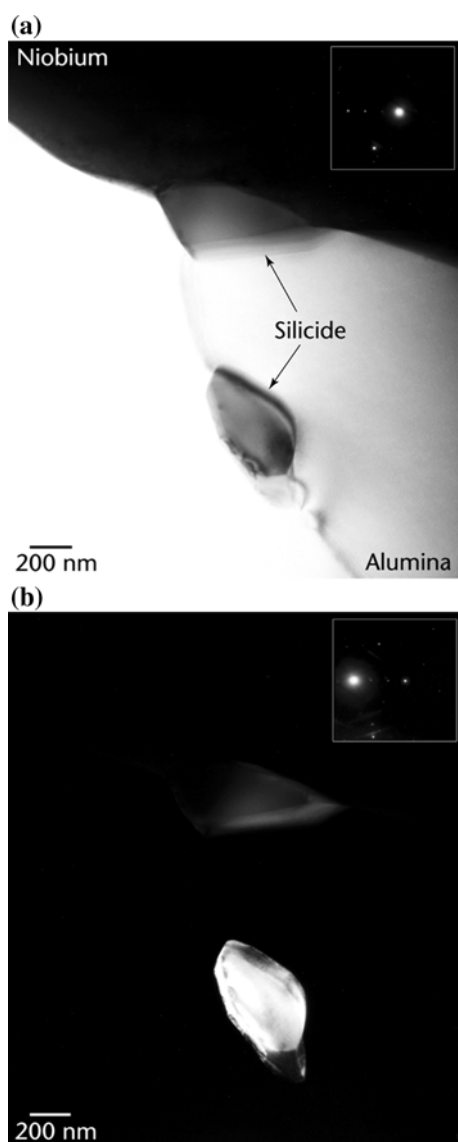
Fig. 8 a Bright-field and **b** dark-field TEM images of a silicide particle at an Al_2O_3 grain boundary

point is that the compositions lie in the two-phase field and the structure is unambiguously that of the Nb_5Si_3 phase. A calculation using the range of measured compositions (including error) gives values of 0.02–0.33 for the expected phase fraction of the $NbSi_2$ phase. Examination of a dozen particles suggests that this phase did not form. Several other factors are likely to contribute to this apparent disparity between the observations and expectations based on equilibrium. The phase diagram assessments (1500, 875, and 800 °C sections) did not include compositions lying in the "Nb_5Si_3–$NbSi_2$" two-phase region. Thus, there is uncertainty in the limits of the Nb_5Si_3 phase stability field in the ternary diagram. However, a more significant source of error will stem from difficulties in obtaining quantitative

EDS data from small, dispersed silicide phases within a matrix phase (surrounding Nb and Al_2O_3), leading to large uncertainty in the measured compositions. This will cause shifts in the apparent compositions of the silicide particles. Previously [20, 69], compositions of binary silicides were determined by assuming an exact stoichiometry to calculate *k*-factors, thus providing a range of compositions that fit this stoichiometry. Furthermore, the analysis of a multiphase specimen in which the electron beam passes through one or more phases will lead to an incorrect measurement of composition for the phases. In prior studies [69] efforts were made to examine only silicides that projected out from the edge of the TEM foil, avoiding the complications of a multiphase analysis. In this study, it was not possible to obtain spectra from isolated silicide particles unless the silicides were at the ceramic–metal interface. The quantitative correction software makes the implicit assumption that the specimen has a composition given by the combination of all the elements present in the spectrum, which will lead to erroneous application of the ZAF corrections [70].

In parallel, one can also compare the findings to those of prior studies of niobium-silicide nucleation and growth involving Nb/Si planar reaction couples [11], bulk diffusion couples of Nb/Si and Nb/$NbSi_2$ [22], or the deposition of thin Nb films onto single-crystal substrates [9], followed by annealing at various temperatures. As discussed by Milanese et al. [22], thin-film studies can provide limited amounts of one or more components, phases may form sequentially rather than simultaneously, and interfaces may affect growth and diffusion. The discussion in the literature of the considerations that enter into determining the first phase to nucleate in thin-film structures [9, 11, 17, 18] provides an example of such effects. Nucleation energetics may favor metastable phases [20] or extend the stability field. Moreover, in the present work the Si source is a silicate phase, the Nb is alloyed with Cu and O, and growth is along either Al_2O_3–Nb or Al_2O_3–Al_2O_3 interfaces. Thus, chemical differences and microstructural factors may also play a role.

As mentioned previously, changes in the bonding temperature (from 1150 to 1400 °C), changes in the atmosphere during bonding or post-bonding anneals (vacuum versus gettered Ar), increases in the Cu film thickness (1.5 to 5.5 μm), and changes in fracture test method (bend versus fatigue tests) all appear to influence the dominant path of crack propagation in these materials, with an overall increase in the average fracture strength and a transition from all interfacial to predominantly ceramic failure for samples using the optimum processing conditions (McKeown et al., unpublished). Depending upon the bonding and test conditions, significant tearing of the Nb foil, propagation of the crack along the ceramic-interlayer

interface, or significant excursions into the Al_2O_3 was observed.

Several studies have revealed that the interfacial silicides tend to form most easily in the finer-grained regions of the Al_2O_3. In view of the bimodal character of the Al_2O_3 grain size, this suggests that a substantial fraction of the total interface could potentially include silicide particles. This is consistent with the relative ease of finding the particles in TEM cross-sections. A reduced milling rate relative to Cu is also expected, which facilitates observation. The microscopy indicates that the Nb_5Si_3 grows both laterally along the ceramic–metal interface and into the Al_2O_3 along grain boundaries. As shown in this study and prior work [6, 7, 52], the silicides do not provide a continuous, low-energy fracture path. The silicides are, however, effective in altering the crack path when fracture occurs at or near the ceramic-interlayer interface.

In cases where the fracture has involved excursions of the crack front into the metal foil, one can speculate that the failure proceeded through the patches of silicide along the ceramic–metal interface that extend into the metal. Nb_5Si_3 is known to be brittle, and the fracture toughness has been reported to be between 2.3–5.5 MPa$\sqrt{m}$ [46, 47]. Equilibration of the silicide with the adjoining niobium foil will increase the Si levels and locally harden the niobium. EDS results are unlikely to be sufficiently accurate to distinguish between a failure that propagates through the silicide, along the interface, or deviates to a limited extent into the Si-saturated niobium.

In assessing the fatigue behavior, Kruzic et al. [6] observed that cracks repeatedly extended into the Al_2O_3 but were drawn back to the interface. It was concluded that although the modulus mismatch between Al_2O_3 and Nb would draw the crack to the interface, the lower intrinsic fatigue-crack propagation resistance of some Al_2O_3 grain boundaries allowed the crack to deviate into the ceramic. Preexistent flaws were implicated as possibly expediting these excursions. It appears possible, based on observations in this study, that in addition to pores or near-interfacial pockets of glassy phase, silicide particles located along grain boundaries could also serve as "preexistent flaws." In addition to having low fracture toughness, the coefficient of thermal expansion of Nb_5Si_3 is reported to be 6.2×10^{-6} K^{-1} [47], and thus lower than that of Al_2O_3 ($\approx 8.2 \times 10^{-6}$ K^{-1}). Both the portions of the Nb_5Si_3 that extend parallel to the Al_2O_3-interlayer interface and the wedge-like particles that extend down the grain boundaries would generate tensile stresses in the Al_2O_3. Since these particles do not extend to any significant depth below the Al_2O_3-interlayer interface, this may be a factor in keeping the cracks in the Al_2O_3 to a substantial degree and preventing more substantial deviations away from the interlayer. The lower interfacial fracture energy of Nb_5Si_3 with

Al_2O_3 (≈ 16 J/m^2) relative to that of Nb_5Si_3 with Nb (≥ 34 J/m^2) [49] may also help to account for crack deviations into the alumina.

A much more limited set of bend tests was conducted in which the finer-grain-size 99.9% pure Al_2O_3 was bonded with Cu/Nb/Cu interlayers for varying times (5 min, 30 min, 6 h) at 1400 °C. For the 6 h samples [55], a limited number of room-temperature tests resulted in exclusively ceramic failure and an average fracture strength of ≈ 360 MPa (versus 240 MPa for the 99.5% pure Al_2O_3). The transition to ceramic failure suggests a substantial strengthening of the ceramic-interlayer interface. Whether this is a consequence of fewer or less severe flaws along or near the interface as a result of grain-size refinement and altered Cu-particle characteristics or whether this may in part be due to the lack of periodic arrays of silicide particles is uncertain. Further studies of this behavior that would improve the statistics would be useful, as would more detailed fracture studies. In a system where fracture can involve a wide range of homophase and heterophase interfaces (Al_2O_3/Nb, Al_2O_3/Nb_5Si_3, Al_2O_3/Cu, Nb/Nb_5Si_3, Nb/Cu, and Nb_5Si_3/Cu), understanding microstructural effects and the character of phases that are present becomes a necessary precursor toward fabricating strong, reliable ceramic–metal interfaces.

Summary

Prior work, based largely on optical and scanning electron microscopy, suggested that Al_2O_3–Nb interfaces processed with single-crystal sapphire or high-purity, polycrystalline Al_2O_3 were free of secondary phases. In contrast, interfaces fabricated with a lower-purity, polycrystalline Al_2O_3 formed Nb silicide particles along the Al_2O_3–Nb interface and Al_2O_3 grain boundaries. In the present work, TEM-based methods were used to examine these interfaces at higher spatial resolution, and to provide a more detailed and complete characterization of the crystallographic and chemical characteristics of secondary phases that were present.

The TEM results confirm the absence of silicides (and other secondary phases) in both the sapphire and high-purity Al_2O_3 samples, and the presence of silicides when lower-purity Al_2O_3 is used. Diffraction analysis of a silicide particle at the Al_2O_3–Nb interface revealed that the silicide was the body-centered tetragonal α-Nb_5Si_3 phase. Energy-dispersive spectrometry of silicides both at and slightly away from the interface showed that the range of Nb:Si ratios would place the composition in the two-phase region between Nb_5Si_3 and $NbSi_2$ on the binary Nb–Si phase diagram at all temperatures from the 1400 °C processing temperature down to room temperature. However,

evidence for a two-phase structure was not found. The silicide incorporates a small amount of Cu, which modifies the phase-stability field, and may extend the stability range of the "α-Nb$_5$Si$_3$" structure. Unfortunately, the only isothermal sections available are at temperatures above (1500 °C) or well below (875 °C, 800 °C) the joining temperature. The ternaries also suggest a multiphase microstructure should form. The difficulties of quantitative EDS for small dispersed phases of the type examined and resulting shifts in the apparent composition of the silicide, as well as the role of kinetic barriers to achieving equilibrium in severely constrained systems, emerge as possible explanations for the disparity. Studies of samples subjected to longer anneals and phase-equilibria studies of relevant Nb–Si–Cu compositions at intermediate temperatures would provide useful insights on the origins of the observed microstructures.

References

1. Elssner G, Reidel S, Pabst R (1975) Prakt Metallogr 12:234
2. Korn D, Elssner G, Fischmeister HF, Rühle M (1992) Acta Metall Mater 40:S355
3. Elssner G, Korn D, Rühle M (1994) Scr Metall Mater 31:1037
4. Cannon RM, Korn D, Elssner G, Rühle M (2002) Acta Mater 50:3903
5. Korn D, Elssner G, Cannon RM, Rühle M (2002) Acta Mater 50:3881
6. Kruzic JJ, Marks RA, Yoshiya M, Glaeser AM, Cannon RM, Ritchie RO (2002) J Am Ceram Soc 85:2531
7. McKeown JT, Sugar JD, Gronsky R, Glaeser AM (2006) Mater Charact 57:50
8. Cahn JW (1956) Acta Metall 4:449
9. Walser RM, Bené RW (1976) Appl Phys Lett 28:624
10. Tsaur BY, Lau SS, Mayer JW, Nicolet M-A (1981) Appl Phys Lett 38:922
11. Ronay M (1983) Appl Phys Lett 42:577
12. Massalski TB, Okamoto H, Subramanian PR, Kacprzak L (eds) (1990) Binary alloy phase diagrams. ASM International, Materials Park, OH
13. Pretorius R (1984) Mater Res Soc Symp Proc 25:15
14. Pretorius R (1990) Vacuum 41:1038
15. Pretorius R, de Reus R, Vredenberg AM, Saris FW (1990) Mater Lett 9:494
16. Pretorius R, Vredenberg AM, Saris FW, de Reus R (1991) J Appl Phys 70:3636
17. Zhang M, Yu W, Wang WH, Wang WK (1996) Thin Solid Films 289:180
18. Zhang M, Wang WK (1998) J Mater Res 13:1373
19. Van Heerden D, Gavens AJ, Foecke T, Weihs TP (1999) Mater Sci Eng A 261:212
20. Grylls RJ, Bewlay BP, Lipsitt HA, Fraser HL (2001) Philos Mag A 81:1967
21. Cheng GM, Qian HY, He LL, Ye HQ (2010) Philos Mag 90:2557
22. Milanese C, Buscaglia V, Maglia F, Anselmi-Tamburini U (2003) Acta Mater 51:4837
23. Mattoso Filho N, Achete C, Freire FL (1992) Thin Solid Films 220:184
24. Zankl R, Malter R (1981) Z Metallk 72:720
25. Pan VM, Latysheva VI, Kulik OG, Popov AG (1982) Russ Metall 3:167
26. Ganglberger E (1968) Monatsh Chem 99:549
27. Subramaniam A, Koch CT, Cannon RM, Ruhle M (2006) Mater Sci Eng A 422:3
28. Simpson YK, Carter CB, Morrissey KJ, Angelini P, Bentley J (1986) J Mater Sci 21:2689. doi:10.1007/BF00551474
29. Ravishankar N, Carter CB (2001) J Am Ceram Soc 84:859
30. Hockey BJ, Wiederhorn SM, Blendell JE, Lee J-S, Kang M-K (2003) J Am Ceram Soc 86:612
31. Avishai A, Scheu C, Kaplan WD (2005) Acta Mater 53:1559
32. Dillon SJ, Tang M, Carter WC, Harmer MP (2007) Acta Mater 55:6208
33. Dillon SJ, Harmer MP (2008) J Am Ceram Soc 91:2314
34. Dillon SJ, Harmer MP, Rohrer GS (2010) J Am Ceram Soc 93:1796
35. Brada MP, Clarke DR (1997) Acta Mater 45:2501
36. Bartlett A, Evans AG, Rühle M (1991) Acta Metall Mater 39:1579
37. Sih GC, Rice JR (1964) J Appl Mech 31:477
38. Rice JR, Sih GC (1965) J Appl Mech 32:418
39. Rice JR (1988) J Appl Mech 55:98
40. Dundurs J (1969) J Appl Mech 36:650
41. Suo Z, Hutchinson JW (1989) Mater Sci Eng A 107:135
42. Hutchinson JW, Mear ME, Rice JR (1987) J Appl Mech 54:828
43. Becker TL, Mcnaney JM, Cannon RM, Ritchie RO (1997) Mech Mater 25:291
44. Ritchie RO, Cannon RM, Dalgleish BJ, Dauskardt RH, McNaney JM (1993) Mater Sci Eng A 166:221
45. McNaney JM, Cannon RM, Ritchie RO (1994) Int J Fract 66:227
46. Carrillo-Heian EM, Unuvar C, Gibeling JC, Paulino GH, Munir ZA (2001) Scripta Mater 45:405
47. Nekkanti RK, Dimiduk D (1990) Mater Res Soc Symp Proc 194:175
48. Zhang LT, Wu JS (1998) Scripta Mater 38:307
49. Shaw L, Miracle D, Abbaschian R (1995) Acta Metall Mater 43:4267
50. Shalz ML, Dalgleish BJ, Tomsia AP, Cannon RM, Glaeser AM (1994) J Mater Sci 29:3678. doi:10.1007/BF00357335
51. Marks RA, Chapman DR, Danielson DT, Glaeser AM (2000) Acta Mater 48:4425
52. Sugar JD, McKeown JT, Marks RA, Glaeser AM (2002) J Am Ceram Soc 85:2523

53. McKeown JT, Sugar JD, Gronsky R, Glaeser AM (2005) Weld J 84:41S
54. Shalz ML, Dalgleish BJ, Tomsia AP, Glaeser AM (1994) J Mater Sci 29:3200. doi:10.1007/BF00356663
55. Marks RA, Sugar JD, Glaeser AM (2001) J Mater Sci 36:5609. doi:10.1023/A:1012565600601
56. Dauskardt R, Lane M, Ma Q, Krishna N (1998) Eng Fract Mech 61:141
57. Sugar JD, McKeown JT, Akashi T, Hong SM, Nakashima K, Glaeser AM (2006) J Eur Ceram Soc 26:363
58. Rühle M, Evans AG (1989) Mater Sci Eng A 107:187
59. Rühle M (1996) J Eur Ceram Soc 16:353
60. Burger K, Mader W, Rühle M (1987) Ultramicroscopy 22:1
61. Florjancic M, Mader W, Rühle M, Turwitt M (1985) J Phys (Paris) 46:129
62. Mader W, Rühle M (1989) Acta Metall 37:853
63. Barin I (1995) Thermochemical data of pure substances. VCH Publishers, New York
64. Perkins RA, Padgett RA (1977) Acta Metall 25:1221
65. Marks RA (2000) MS Thesis, University of California, Berkeley
66. Villars P, Calvert LD (1991) Pearson's handbook of crystallographic data for intermetallic phases. ASM International, Materials Park, OH
67. Schlesinger ME, Okamoto H, Gokhale AB, Abbaschian R (1993) J Phase Equilib 14:502
68. Geng J, Tsakiropoulos P, Shao GS (2007) Intermetallics 15:69
69. Cockeram B, Saqib M, Omlor R, Srinivasan R, Matson LE, Weiss I (1991) Scripta Metall Mater 25:393
70. Russ JC (1984) Fundamentals of energy dispersive X-ray analysis. Butterworths & Co, Ltd, London
71. Villars P, Prince A, Okamoto H (eds) (1995) Handbook of ternary alloy phase diagrams. ASM International, Materials Park, OH